Research Square

Preprints are preliminary reports that have not undergone peer review.
They should not be considered conclusive, used to inform clinical practice,
or referenced by the media as validated information.

Satellite evidence of fertilizer-driven, temperature-dependent ammonia emissions

Mauri Rosiers

mauri.rosiers@ulb.be

Université libre de Bruxelles (ULB) https://orcid.org/0009-0003-9922-429X

Martin Van Damme

Universite Libre de Bruxelles (ULB)

Lieven Clarisse

Université libre de Bruxelles https://orcid.org/0000-0002-8805-2141

Mark Sutton

UK Centre for Ecology & Hydrology https://orcid.org/0000-0002-1342-2072

Camille Viatte

Sorbonne Université, UVSQ, CNRS, LATMOS/IPSL

Cathy Clerbaux

LATMOS/IPSL, Sorbonne Université, UVSQ, CNRS https://orcid.org/0000-0003-0394-7200

Anne-Claude Romain

Université de Liège https://orcid.org/0000-0002-7371-9580

Pierre Coheur

Universite Libre de Bruxelles (ULB)

Article

Keywords:

Posted Date: October 26th, 2026

DOI: https://doi.org/10.21203/rs.3.rs-11278482/v1

License: This work is licensed under a Creative Commons Attribution 4.0 International License.
Read Full License

Additional Declarations: There is **NO** Competing Interest.

Satellite evidence of fertilizer-driven, temperature-dependent ammonia emissions

Mauri Rosiers[1,2*], Martin Van Damme[1,3], Lieven Clarisse[1], Mark A. Sutton[4], Camille Viatte[5], Cathy Clerbaux[1,5], Anne-Claude Romain[2], Pierre Coheur[1]

[1*]Université libre de Bruxelles, Spectroscopy, Quantum Chemistry and Atmospheric Remote Sensing (SQUARES), ULB-BLU Space Research Center, Av. Franklin Roosevelt 50, Brussels, 1050, Belgium.
[2]Université de Liège, Sensing of Atmospheres and Monitoring (SAM) Laboratory, UR Spheres, Department of Environmental Science and Management, Faculty of Sciences, Av. de Longwy 185, Arlon, 6700, Belgium.
[3]Royal Belgian Institute for Space Aeronomy, Av. Circulaire 3, Brussels, 1180, Belgium.
[4]UK Centre for Ecology and Hydrology, Edinburgh Research Station, Bush Estate, Penicuik, Midlothian EH26 0QB, United Kingdom.
[5]Sorbonne Université, UVSQ, CNRS, LATMOS/IPSL, 4 Place Jussieu, Paris, 75005, France.

*Corresponding author(s). E-mail(s): mauri.rosiers@ulb.be;
Contributing authors: martin.van.damme@ulb.be; lieven.clarisse@ulb.be; ms@ceh.ac.uk; camille.viatte@latmos.ipsl.fr; cathy.clerbaux@latmos.ipsl.fr; acromain@uliege.be; pierre.coheur@ulb.be;

Abstract

Agricultural ammonia (NH_3) emissions are strongly influenced by environmental conditions and management practices, yet how fertilizer type shapes the temperature response of volatilization at large scales remains poorly understood. Here we show, using a 16-year record of daily NH_3 total columns from the Infrared Atmospheric Sounding Interferometer, that the dependence of atmospheric NH_3 on skin temperature diverges into two fundamentally different responses. In regions

less reliant on urea, NH_3 columns increase monotonically with skin temperature, matching the classical process-based representation of NH_3 volatilization. In urea-dominated regions, by contrast, NH_3 columns rise quasi-exponentially to a characteristic breakpoint between 310 and 318 K, above which they decline sharply. This discontinuity, revealed here for the first time using a large observational dataset, is consistent across urea-dominated regions. We hypothesize that this discontinuity reflects a temperature-limited NH_x supply in urea-dominated systems, potentially mediated by urease-catalyzed hydrolysis and modulated by local environmental conditions. These findings identify fertilizer type, soil characteristics, and climate variability as key drivers of NH_3 volatilization, and suggest that their combined effects must be represented in models to improve emission predictions and anticipate climate impacts on air quality and nitrogen deposition.

Keywords: Ammonia volatilization, agricultural emissions, satellite remote sensing, urea, fertilizer

Since the 1930s, the use of nitrogen (N) fertilizers has risen sharply to meet growing food demand, making modern agriculture critically dependent on them [1]. Yet, over 80% of anthropogenic reactive nitrogen is lost to the environment [2], with ammonia (NH_3) emissions from fertilized soils and livestock excreta among the largest of these losses [2, 3]. Atmospheric NH_3 contributes to the formation of fine particulate matter ($PM_{2.5}$) [4], which is associated with cardiovascular and respiratory diseases, and caused an estimated 4.7 million premature deaths in 2021 alone [5]. Beyond air quality, reactive nitrogen delivered to surface compartments via atmospheric deposition and hydrological runoff accelerates soil acidification and eutrophication, threatening biodiversity across terrestrial and aquatic ecosystems [6, 7]. Despite these well-documented impacts, atmospheric NH_3 columns have continued to rise over the past two decades [8], underscoring how poorly the drivers of NH_3 emissions are currently understood and constrained.

The dominant NH_3 emission process from these agricultural sources is volatilization from the soil to the atmosphere. Warming is expected to enhance this process by accelerating both gas-phase conversion and atmospheric release. In soils, NH_3 is in acid–base equilibrium with ammonium ($NH_4^+ \rightleftharpoons NH_3 + H^+$), so that lower soil acidity (higher pH) and warming shift this balance toward free NH_3, increasing the soil emission potential $\Gamma_{soil} = [NH_4^+]/[H^+]$ [9]. Exchange with the atmosphere is further governed by Henry's law, under which NH_3 solubility decreases with temperature. Soil moisture modulates the magnitude of this exchange, retaining NH_3 in solution when soils are wet but promoting its release as they dry, a transition that itself typically accompanies warming [10–13]. Together, these thermodynamic controls imply a non-linear yet monotonic increase of NH_3 exchange with temperature [11, 13, 14]. Further details on the equilibria at play and on state-of-the-art volatilization models are provided in Supplementary Information. Key implementations of this process include canopy compensation-point formulations [9, 13] and temperature-correction approaches [14], which both reproduce this monotonic thermal response.

These parameterizations currently serve as the standard framework for representing soil–atmosphere fluxes in chemistry transport and Earth system models [15–18].

Building on these formulations, Abeed et al. [19] used satellite NH_3 columns from the Infrared Atmospheric Sounding Interferometer (IASI), a hyperspectral infrared sounder aboard the Metop satellites that has provided twice-daily global measurements of atmospheric NH_3 since 2007 [8], to characterize Γ_{soil} over Europe, assuming that the short atmospheric lifetime of NH_3 (hours to days) allows column abundances to be used as a proxy for local surface emissions. That study demonstrated the feasibility of deriving process-level information from space, but was restricted to a single month at the onset of the growing season and to a region where temperatures rarely exceed 310 K, without differentiating fertilizer type. Extending this approach globally across a wider temperature range, and stratifying regions by their urea reliance, IASI NH_3 observations reveal a striking asymmetry: whereas non-urea dominated regions exhibit the monotonic response of NH_3 to skin temperature (T_{skin}) predicted by current parameterizations, urea-dominated regions show a quasi-exponential rise up to a characteristic breakpoint temperature (T_b), above which NH_3 columns decline sharply. This suggests that fertilizer type could introduce a temperature-sensitive control on NH_3 release that is not captured by current parameterizations.

In urea-dominated systems, NH_x (NH_3 + NH_4^+) availability largely depends on the hydrolysis of urea, catalyzed by the soil enzyme urease. Unlike non-urea fertilizers that supply a substantial fraction of N directly as NH_x, urea-based fertilizers must first be hydrolyzed before contributing to NH_3 volatilization [20]. This requirement is especially important, as urea dominates global synthetic fertilizer use [21], and a substantial fraction of N excreted by livestock is also in the form of urea [3], so the same hydrolysis step governs both sources. This enzymatic step adds a temperature-dependent biological control on NH_x formation that is absent when N is already present in ammoniacal form.

In contrast to *in vitro*, where the temperature response of urease is governed by enzyme-level (Arrhenius-type) kinetics [22, 23], the field-scale urease optimum depends fundamentally on the size of the active enzyme pool [24]. This pool reflects a balance between two processes: the persistence of existing enzymes and its ongoing production by urease-producing bacteria, whose growth peaks between 303 and 308 K and is suppressed above ∼313 K [25]. Enzyme persistence, in turn, declines steeply with temperature: urease half-life shortens from 16–32 days at 277 K to only 2–6 hours at 343 K [26]. As warming accelerates this loss while simultaneously suppressing microbial replenishment, the active enzyme pool is expected to become severely restricted above ∼308–313 K [25, 26]. We therefore hypothesize that this urease supply limitation might impose a thermal ceiling on NH_3 release in urea-dominated systems.

Here, we use 16 years of daily IASI NH_3 observations across diverse global agricultural regions to investigate how fertilizer type shapes large scale NH_3–T_{skin} responses. We contrast the annual and seasonal thermal dynamics of urea and non-urea dominated regimes, examine drought–rewetting pulses as an additional volatilization mechanism, and outline the broader implications for global NH_3 emission modeling.

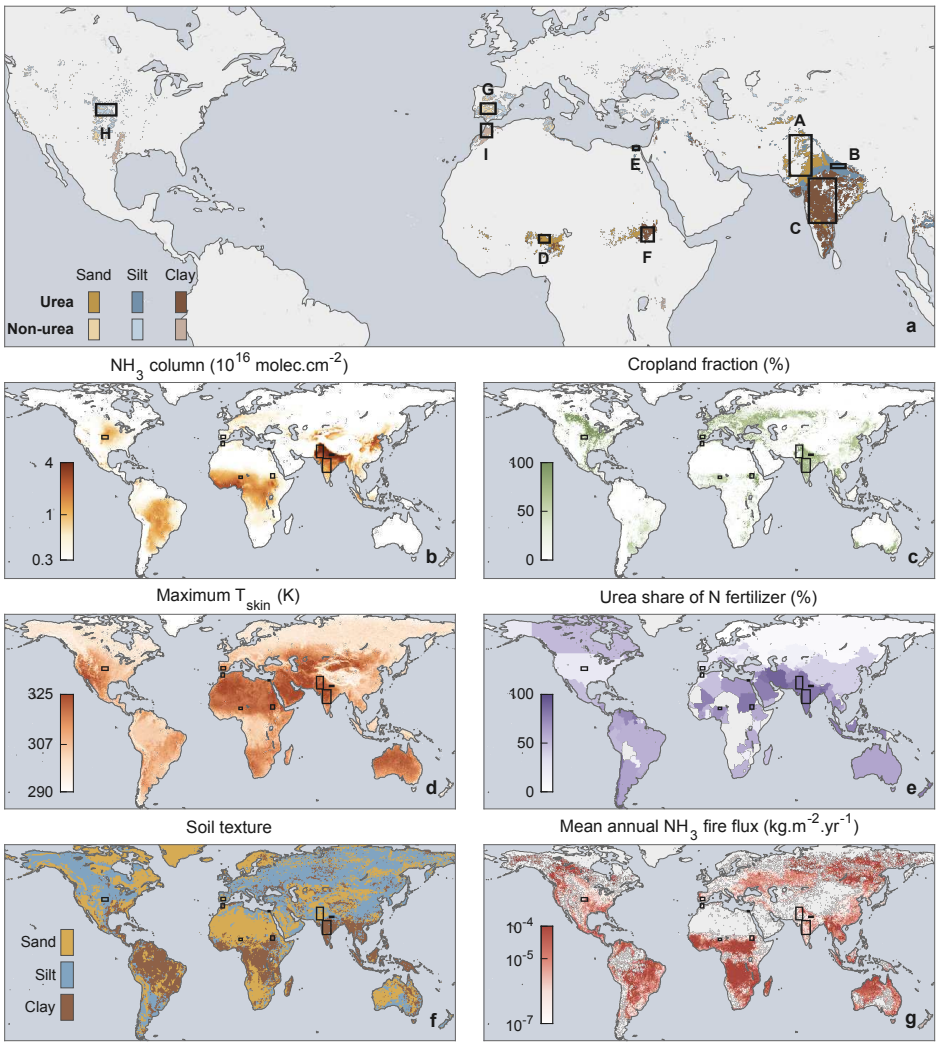


Fig. 1 Selection of the nine agricultural regions. a, Agricultural regions colored by dominant soil texture and by fertilizer regime, with the nine selected regions (A–I) outlined. **b**–**g**, 16-year (2008–2023) mean morning IASI NH_3 column (molec.cm^{-2}) [27], cropland fraction (%) [28], maximum T_{skin} (K) [27], national urea share of total synthetic N fertilizer (%) [21], dominant soil texture [29] and mean annual NH_3 fire flux (kg m^{-2} yr^{-1}) [30], respectively. These datasets were used to select the nine regions in **a**, following the criteria laid out in the Methods.

Study regions and analytical approach

Building on the rationale introduced above, agricultural regions were classified using national fertilizer statistics from IFASTAT [21], based on the mean contribution of urea to total synthetic N use over 2008–2023. We defined urea-dominated systems

as regions with urea $\geq$ 65% (for most regions it is $\sim$80%) and non-urea dominated systems as regions with urea $\leq$ 40% (typically below 30%) (Methods).

We selected nine representative cropland-intensive regions (Fig. 1a) showing elevated NH_3 columns to contrast fertilizer regimes across sandy, silty and clayey soils (Fig. 1). Comparing these distinct soil textures explicitly accounts for their different capacities to buffer pH and regulate emissions; more precisely, clayey and, to a lesser extent, silty soils strongly retain NH_3, whereas sandy soils favor rapid release [31]. Additionally, we required T_{skin} to frequently exceed 310 K to ensure a sufficiently large dynamic temperature range. Regions significantly affected by biomass burning, which is a known source of NH_3 [30, 32], have been excluded. For each region, we constructed annual and monthly NH_3–T_{skin} curves (Figs. 2 and 3), from which we derived two diagnostics: the breakpoint temperature T_b, above which the temperature dependence reverses, and the pre-breakpoint Q_{10}, the factor by which NH_3 increases for a 10 K rise (Methods).

NH_3–T_{skin} relationships

Figure 2 compares normalized, 16-year aggregated IASI NH_3–T_{skin} observations for two distinct agricultural regions (281–331 K) against theoretical baselines (dashed and dash-dotted lines) [9, 14]. As introduced, these reveal a striking contrast dictated by fertilizer type: in the non-urea dominated region (Spain, region G; blue curve), NH_3 columns increase quasi-monotonically, whereas in the urea-dominated region (South Asia, region A; red curve), columns rise steeply up to 310 K before rapidly declining. The appearance of this breakpoint has, to the best of our knowledge, not been reported before and seems consistent for urea-dominated regions, although subject to significant seasonal dependence. Figure 3 shows the NH_3–T_{skin} curves for all nine regions, annual and monthly, with T_b and the pre-breakpoint Q_{10} calculated wherever possible and reported in Table 1 and Supplementary Tables 1 and 2. We first describe the annual relationships, then how seasonality modulates them.

In the urea-dominated regions (A–F), annual mean NH_3 columns (Fig. 3; black lines) increase with T_{skin} up to a characteristic breakpoint, before declining at temperatures above $\sim$310–318 K (Fig. 3; two uppermost rows). A sustained turnover is resolved in four of the six urea-dominated regions (A, B, D, E) and in none of the three non-urea dominated regions; the two exceptions, regions C and F, are discussed below. The discontinuity in the annual curves is particularly pronounced in the South Asian regions: regions A (NW Indo-Gangetic Plain; hereafter NW IGP) and B (central IGP) show steep pre-breakpoint increases with Q_{10} values of 2.39 and 1.92, respectively, which are followed by sharp declines above T_b: NH_3 columns in region A fall by nearly half over the 20 K above the breakpoint, and by about a quarter in region B, whose sampled range ends 10 K above its T_b (Fig. 3). Region C (Deccan Plateau) shows the same initial rise, with a smaller Q_{10} (1.23) and a visible maximum near 317 K. However, it diverges fundamentally from the other two regions under extreme heat: above 323 K the curve rises again, and by the top of the sampled range it has returned to, and slightly exceeded, its earlier maximum. Because this decline is not sustained, no annual T_b is reported for region C, although individual months do resolve

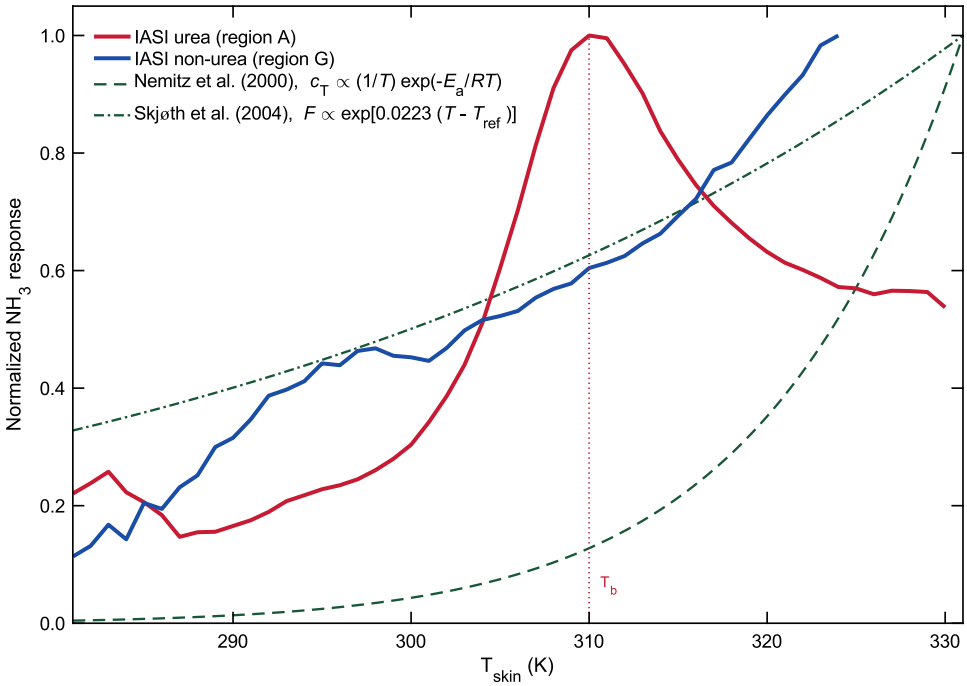


Fig. 2 Temperature-dependent NH_3 volatilization responses. Response functions from two widely used parametrizations (dashed and dash-dotted lines) [9, 14], are presented alongside annual IASI-derived normalized NH_3 columns as a function of T_{skin} for two contrasting agricultural regions: a urea-dominated region in South Asia (NW Indo-Gangetic Plain, region A; red) and a non-urea dominated region in Spain (region G; blue). Both parametrizations are plotted as functions of T_{skin}, with all other terms held constant. Nemitz et al. [9] give the temperature dependence of the canopy compensation point $c_T \propto (1/T)\exp(-E_a/RT)$, where T is temperature, R the gas constant and $E_a/R = 10378\,\mathrm{K}$ the effective enthalpy combining the NH_4^+/NH_3 dissociation and Henry's law equilibria, while Skjøth et al. [14] use the empirical form $F \propto \exp[0.0223\,(T - T_{ref})]$, in which T_{ref} is a reference temperature and the coefficient $0.0223\,\mathrm{K}^{-1}$ was fitted to measured emission data. All curves are normalized at their maximum for visual comparability. The breakpoint temperature (T_b) is shown for the urea-dominated region, indicating where the temperature dependence reverses.

one (Supplementary Table 2). This enhancement is discussed below. Regions D and E display the same unimodal behaviour, with T_b of 318 and 311 K. In region F (Sudan) the sampled range begins on the warm plateau, so no rising branch and no annual T_b can be resolved, although the column declines monotonically above 312 K and three individual months do turn over (Supplementary Table 2). Note that Q_{10} values in urea-dominated regions fall within or just below the range of 1.5–3 reported for agricultural soils [13].

A plausible interpretation of the unimodal shape in regions A–F is that above a critical temperature the active urease pool is depleted faster than it can be replenished, constraining hydrolysis and ultimately the NH_x available for volatilization. This interpretation is supported by the systematic clustering of breakpoint temperatures within the 310–318 K window, consistent with the expected temperature range for field-scale

optima governed by turnover of the active enzyme pool rather than by enzyme kinetics alone [24, 25, 33]. Crucially, this interpretation is also supported by the absence of a unimodal response in non-urea dominated regions (G–I), as the NH_3 columns in these regions increase almost monotonically over the entire temperature range (Fig. 3, bottom panels), more consistent with theoretical, purely physicochemical, volatilization schemes, while showing lower annual Q_{10} values than most urea-dominated regions considered here (1.48–1.74). This class contrast extends to the full set of twenty regions analyzed here, including those of Supplementary Figs. 1–3, and holds without reference to any breakpoint: the more a region relies on urea, the more its NH_3 columns decline over the warmest quarter of its own sampled temperature range ($\rho = -0.69$, $n = 20$, $p = 0.001$; Methods).

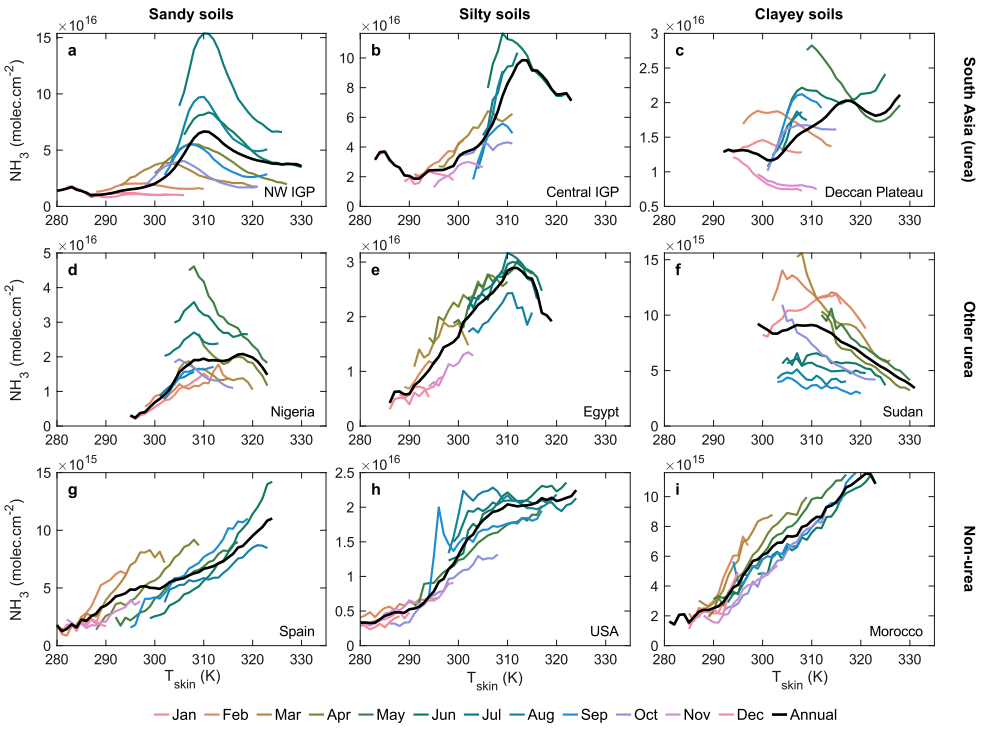


Fig. 3 Monthly and annual mean NH_3–T_{skin} relationships for the nine agricultural regions. Regions are grouped by dominant soil type and fertilizer regime (as defined in Fig. 1). From left to right, panels represent sandy, silty and clayey soils. From top to bottom, rows represent South Asian urea-dominated regions, other urea-dominated regions (Nigeria, Egypt, Sudan) and non-urea dominated regions (Spain, USA, Morocco). Colored curves show monthly means; black curves show the annual mean. Months corresponding to peak fire activity have been excluded on a region-specific basis, from the annual as well as the monthly curves, to minimize the contribution of non-agricultural sources (Methods).

These annual NH_3–T_{skin} relationships, however, aggregate across substantial seasonal variability. The monthly curves (colored lines in Fig. 3) show that this variability

Table 1 Characteristics of the nine selected agricultural regions. Dominant soil texture, urea contribution to total synthetic N fertilizer use, the Q_{10} of the rising branch, and the breakpoint temperature T_b (Methods). Bracketed values are the range across the calendar months, each fitted separately; where only one month satisfies the reporting criteria, no range is given. Because curve fits depend on the sampled temperature range, annual parameters are not simple averages of monthly values. Years span broader extremes, meaning the annual Q_{10} and T_b can fall outside the monthly range. Entries are left blank where the sampled temperature range, the number of observations or the width of the confidence interval do not support an estimate. Confidence intervals on all values are returned by the analysis code (Code availability).

Region (Soil Type)	Urea	Q_{10}	T_b
Northwest IGP (A; sandy soil)	81.6%	2.39 (1.55–2.08)	310 K (298–311 K)
Central IGP (B; silty soil)	80.9%	1.92 (1.85–2.29)	313 K (294–309 K)
Deccan Plateau (C; clayey soil)	80.9%	1.23	—[a]
Nigeria (D; sandy soil)	70.8%	1.81 (1.62–3.47)	318 K (307–308 K)
Egypt (E; silty soil)	68.1%	1.99 (1.27–1.54)	311 K (310 K)
Sudan (F; clayey soil)	81.5%	—[b]	—[b] (307–311 K)
Spain (G; sandy soil)	29.6%	1.48 (1.81–2.66)	—
USA (H; silty soil)	23.5%	1.74 (1.24–2.18)	—
Morocco (I; clayey soil)	19.3%	1.72 (1.55–3.81)	—

[a] NH_3 columns in region C recover above 323 K to their earlier maximum and slightly beyond it, so the decline is not sustained and no annual T_b is reported. [b] The sampled temperature range in region F does not extend below the plateau of the annual curve, so neither a rising branch nor a turnover can be resolved; the column declines monotonically above 312 K, and three individual months do turn over (Supplementary Table 2).

is mechanistically informative, most visibly as a systematic seasonal shift of T_b in urea-dominated regions. In South Asia, we observe that peak agricultural months (April–May to September–October) exhibit consistently unimodal responses with maxima around 306–311 K in regions A and B, followed by rapid declines, even during periods of peak NH_3 columns, when N inputs are likely highest. During drier, and less agriculturally active months (November–April), breakpoints shift to lower temperatures and NH_3 columns are reduced. Curves from this period should, however, be interpreted cautiously, as abundances approach the IASI detection limit [34]. In region C, the monthly curves retain the unimodal form below ∼315 K, but show high-temperature enhancements in May–June above this temperature threshold that coincide with the first monsoon rains and a pulse-like response to soil rewetting (examined below).

The seasonal shift of breakpoint temperatures in regions A–C is difficult to reconcile with the hypothesis of a fixed optimum temperature for field-scale urease activity alone. Under warm (∼303–313 K), nutrient-rich, and moist conditions (June–October in South Asia), the urease pool is near its optimal state and actively renewed, so that replenishment matches, or even dominates over, enzyme degradation, setting the effective T_b [24, 26], consistent with the ∼310–318 K range observed in the annual curves. However, in drier, less agriculturally active months, reduced soil moisture and nutrient availability limit microbial growth and enzyme synthesis [33, 35–37], severely restricting the capacity for enzyme renewal. In this suppressed state, the temperature at

which heat-induced enzyme degradation outpaces replenishment is likely much lower. Such a reduction in urea hydrolysis potential could ultimately drive an earlier decline in NH_x availability, translating into the downward shift of T_b observed in regions A–C during November–April. Consistent with this, Feng et al. [33] found that urease activity tracks urease-producing microbial diversity more strongly in wet than dry soils, implying that the microbial community's capacity to sustain urease production indeed weakens under dry conditions. A further consequence of this interpretation is testable. If the size of the ammoniacal nitrogen pool sets the temperature at which emission can no longer be sustained, then the months that turn over at a higher T_b should also reach a higher NH_3 maximum, the same larger pool producing both. Across the eight months of region A that individually resolve a turnover, spanning 13 K in T_b, the two are indeed correlated ($r = 0.90$ between T_b and the logarithm of the monthly maximum).

Across the urea-dominated regions outside South Asia (D–F), the monthly curves behave similarly but often sample a narrower temperature range, such that some individual months might only capture the pre- or post-breakpoint branch (Fig. 3). For instance, in persistently warm climates (e.g., Sudanese region F) the low-temperature branch is not well monitored, while in the other regions temperatures above 320 K are rarely encountered. By contrast, the regions that rely little on urea (G–I) remain monotonic throughout the year, varying month to month in amplitude rather than in curve shape, with monthly Q_{10} values from 1.2 to 3.8, largely within the reported range [13]. The supplementary regions show similar behavior across the different soil types, within each fertilizer class (Supplementary Figs. 1–3, and Supplementary Tables 1–3). These seasonal patterns cannot, however, explain the episodic, anomalously high NH_3 columns measured well above T_b (region C in May–June; Fig. 3).

Drought–rewetting effects on NH_3 variability

In Figure 4, we examine how rainfall, soil moisture, and T_{skin} correlate with the NH_3 columns measured from IASI. This is done for 2021 in region A (NW IGP), where NH_3 columns and observation density are highest and the sporadic high-temperature enhancements most pronounced. A single year is needed because 16-year aggregation largely masks these short-lived weather-coupled pulses. The seasonal cycle of soil moisture and rainfall shows that the region experiences a clear transition from hot and dry pre-monsoon conditions to monsoon-humid conditions in early July (Fig. 4a). From that period on, soil moisture rises rapidly (Fig. 4a; blue curve) and NH_3 columns increase in parallel (Fig. 4b; black curve).

More precisely, NH_3 columns peak at the end of July, when soils are rewetted and T_{skin} has already passed its annual maximum. The temporal alignment between these parameters is consistent with a Birch-like response, in which rewetting after prolonged drought stimulates microbial activity and N turnover, increasing the pool of volatilizable NH_x in warm soils [40, 41]. In South Asian agricultural systems, particularly across the NW IGP, the monsoon (kharif) cropping season could contribute independently. Rice seedlings are planted into flooded fields in the weeks after the monsoon rains arrive [42], and in Indian Punjab, for example, legislation prohibits planting

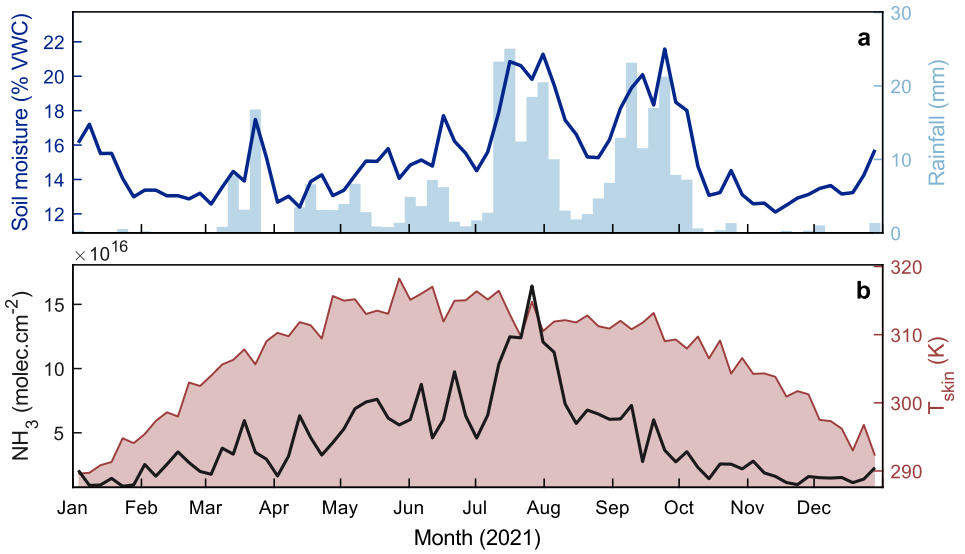


Fig. 4 Evidence for drought–rewetting-driven NH_3 pulses across the NW Indo-Gangetic Plain (region A) in 2021. a, Soil moisture (volumetric water content, %) from the ESA CCI Soil Moisture COMBINED product (dark blue line, left axis) [38] and accumulated rainfall from CHIRPS v3 (light blue bars, right axis) [39]. **b**, NH_3 total columns (black line, left axis) and T_{skin} (red shading, right axis). All series are shown as 5-day (pentad) values; month labels indicate the start of each month.

rice in the drier months before the monsoon [43]. Soil rewetting, fertilizer application and still-high T_{skin} therefore fall in the same weeks, which can amplify the soil's NH_3 emission potential [12]. Both mechanisms could contribute to the observed pulses, and a single year in one region cannot separate them. After the late-July maximum, NH_3 columns decline markedly despite persistent rain throughout August–September, while soils remain wet and T_{skin} stays elevated. Neither soil moisture nor temperature accounts for this decline, which could instead be a signature of rapid NH_x pool depletion following an initial burst of mineralization and microbial activity at monsoon onset [40, 41]. Consistent with this interpretation, Krichels et al. [12] showed that rewetting of dry soils can trigger significant NH_3 volatilization losses (up to ∼30-fold higher at the most alkaline site than at the most acidic one), with fluxes up to ∼3-fold higher when water and NH_4^+ are added simultaneously.

The same processes may also explain the NH_3 enhancements observed in region C, although that particular region proves more difficult to investigate due to its size and significant monsoon cloud cover. Whether such short-lived pulses occur more widely remains to be tested, but the conditions that produce them are not unique to South Asia and could arise in other intensive agricultural areas wherever prolonged drought under warm conditions precedes intense rainfall events.

Discussion

In interpreting the data, several caveats should be acknowledged. First, satellite-derived NH_3 columns do not uniquely isolate surface emissions: their temperature dependence may also reflect variations in atmospheric lifetime, transport, vertical mixing, and retrieval sensitivity. Second, our urea versus non-urea dominated classification is based on mineral fertilizer statistics and should be interpreted as a coarse proxy for dominant synthetic fertilizer form rather than total agricultural N input. Seasonal and regional differences in fertilizer timing and management, crop type, and irrigation may also co-vary with temperature and contribute to the observed patterns. While the satellite-derived temperature dependence cannot be taken as a direct measure of urease activity, it provides a process-level interpretation of a robust observational record. The strength of the result lies in the consistent contrast between urea- and non-urea dominated systems, the clustering of breakpoint temperatures in urea-dominated regions, and the seasonal modulation of the NH_3–T_{skin} curves, with episodic drought–rewetting pulses adding to this in some regions.

Our findings could have direct implications for NH_3 emission modeling. Most current chemistry-transport and Earth-system models assume that warming increases NH_3 volatilization monotonically through its effects on partitioning and transfer. Our results indicate that this is adequate for systems in which N is supplied directly in ammoniacal form, but does not hold in regions where N is applied as urea, which must first be hydrolyzed in soil. In such systems, warming does not uniformly amplify agricultural NH_3 burdens: the response depends on fertilizer regime, hydro-climate and soil context, and can even decline significantly beyond a given T_b. Such behavior should therefore be represented more consistently in models to better predict future NH_3 burdens and the $PM_{2.5}$, N-deposition and ecosystem impacts they drive. This would in turn help design management strategies to reduce agricultural NH_3 losses under warming climates.

Methods

IASI NH_3 and T_{skin} data

The Infrared Atmospheric Sounding Interferometer (IASI), deployed aboard the Metop satellites, provides twice-daily global measurements of atmospheric temperature and humidity, trace-gas abundances and surface temperature. Its spatial resolution (12 km at nadir), swath width (2100 km), and radiometric and spectral performance (0.5 cm^{-1} apodized spectral resolution with low noise) [44] have been instrumental to characterize the spatiotemporal variability and budget of atmospheric NH_3 [8, 45, 46], as well as many other trace gases [47]. IASI measurements have been used to identify global NH_3 hotspots, assess seasonal and inter-annual variability, analyze long-term trends and support source attribution studies [8, 32, 34, 45, 46]. Using the data record provided by the IASI instruments on Metop-A (2008–2020) and Metop-B (2013–2023), we constructed long-term NH_3–T_{skin} relationships over selected agricultural regions. NH_3 total columns were taken from version 4 of the Artificial Neural Network for IASI (ANNI) products, which improve temporal consistency relative to earlier versions

[27], while T_{skin} was retrieved using a dedicated neural network [27]. To minimize uncertainty in the NH_3 retrievals, only morning IASI observations were retained and a maximum cloud-cover threshold of 10% was applied. Restricting the analysis to daytime observations increases sensitivity to the boundary layer because of the larger thermal contrast between the surface and the atmosphere [34, 48].

All quality-filtered NH_3 observations from 2008 to 2023 were aggregated into 1 K T_{skin} bins centered on integer kelvin values (279.5–339.5 K), and the mean NH_3 column in each bin was used to construct the NH_3–T_{skin} relationships. Bins containing less than 2 % of the maximum bin population, or fewer than 20 observations, were excluded to ensure statistical robustness. Monthly relationships were derived using the same binning approach but restricted to individual calendar months. Annual NH_3–T_{skin} curves therefore represent the mean NH_3 column per 1 K bin across all daily observations, rather than averages of monthly means, thereby preserving full temporal sampling while giving greater weight to periods with higher observational density.

Breakpoint temperature and Q_{10}

For each binned curve, annual and monthly, two quantities were derived independently: the breakpoint temperature T_b and the pre-breakpoint Q_{10}. No value was inherited between an annual curve and its months; every curve was analyzed on its own.

T_b was defined as the skin temperature at which the binned NH_3 column reaches its maximum. Candidate temperatures were restricted to the plateau of the curve, taken as the bins lying within 5 % of the maximum of the column smoothed over three 1 K bins in logarithmic space, and T_b was taken as the highest observed bin within that plateau. T_b is reported as the center of that 1 K bin, which sets its resolution. Smoothing determines which bins are plausible maxima, so that a single noisy bin cannot set T_b, while the reported value remains a temperature at which NH_3 was measured to be highest. A T_b was retained only where the column rises into that maximum with at least 3 K of sampling below it, where observations extend at least 5 K above it, where the column falls by at least 15 % between T_b and the upper end of the sampled range, and where that decline is sustained rather than followed by a recovery.

Q_{10} is the factor by which the NH_3 column changes for a 10 K rise in skin temperature, $Q_{10} = \exp(10\,b)$, with b the slope of a log-linear fit to the rising branch of the curve, from its coldest retained bin up to and including T_b where a turnover is resolved, and across the whole sampled range where none is. Weighting each bin by its IASI observation count ensures the densely sampled core of the temperature range dictates the slope, preventing sparse data at the extremes from skewing the fit. A Q_{10} was reported only where the fit was well determined. This required at least eight retained bins on the rising branch and a fitted span of at least 8 K. In addition, a fit had to draw on at least 200 individual observations summed over those bins, reach a population-weighted R^2 of at least 0.50, and return a 95 % confidence interval narrower than 45 % of the estimate.

The annual and monthly curves of a region are fitted independently, and they do not cover the same temperatures. As noted above, an annual curve is a mean over all observations rather than an average of monthly means, so it extends from the coldest

1 K bin reached in any month to the warmest reached in any, while a single month covers only its own part of that interval. The annual Q_{10} is therefore not an average of the monthly values and does not necessarily lie within their range. The same holds for T_b. The warm end of an annual curve is populated only by the months that reach those temperatures, so the annual maximum describes the warm-season part rather than the mean of the monthly maxima, and may lie above the highest of them. A monthly value contributes to the reported range only where its fit describes a rising branch; months in which NH_3 declines across their whole sampled range are excluded. Where only one month satisfies these conditions, the single value is not reported as a range. Curves failing any criterion are not reported.

Comparison between fertilizer classes

To compare the two fertilizer classes without relying on a breakpoint, a Q_{10} was fitted in the same way over the warmest quarter of each region's own sampled temperature range. This gives one value for every region, including those in which no turnover is resolved. The median is 0.81 in the urea-dominated regions and 1.56 in the others (exact two-tailed Mann–Whitney U test, $p = 4 \times 10^{-5}$, ten regions in each class), and ranking the twenty regions by this value and by their urea share gives a Spearman correlation of -0.69 ($p = 1 \times 10^{-3}$, from 20,000 random reshufflings of the ranks). The correlation uses no class boundary, and regions were classified from fertilizer statistics before any curve was fitted.

Agricultural region selection

Agricultural regions were classified using national-scale synthetic N fertilizer consumption statistics from IFASTAT [21]. For each country, synthetic N fertilizer use over 2008–2023 was compiled and the mean contribution of urea-based fertilizers was calculated relative to total synthetic N consumption. The resulting urea fractions should be interpreted as conservative estimates, as mixed fertilizer formulations such as urea ammonium nitrate (UAN) and NP(K) blends were not (partially) attributed to urea-based fertilizers because their chemical composition varies substantially between products and regions, preventing consistent categorization. Organic N inputs, including animal excreta, were also excluded as IFASTAT does not provide systematic or spatially resolved information for these sources, despite the fact that a substantial fraction of reactive nitrogen in animal excreta originates from urea [3]. Based on these fertilizer-use statistics, two regional classes were defined: (i) urea-dominated regions, where urea-based fertilizers account for at least 65% of total synthetic N input, and (ii) non-urea dominated regions, where the urea contribution does not exceed 40%. These thresholds were chosen to ensure a separation between urea-dominated and non-urea dominated systems while minimizing ambiguous intermediate cases, although some overlap and classification uncertainty is unavoidable in practice. However, it should be underlined that for the nine regions described in the paper, the separation is substantial, with a $\sim$50% difference in urea usage between the two classes. The selected regions corresponding to these classes are shown in Fig. 1.

To ensure spatial consistency across all datasets, gridded data were mapped onto a common regular latitude–longitude grid at $1/12^\circ \times 1/12^\circ$ resolution. Agricultural relevance was assessed using cropland information from the Global Land Cover-SHARE (GLC-SHARE) database [28]. Cropland intensity was defined as the fraction of each grid cell classified as cropland, and only grid cells with a cropland fraction of at least 40% were retained. Within each candidate country, contiguous agricultural clusters satisfying the fertilizer and cropland criteria were identified, and rectangular bounding boxes were defined to encompass the dominant high-NH_3 agricultural cores while aiming to avoid major urban or water bodies. Soil properties were obtained from the Harmonized World Soil Database (HWSD) v2.0 [29]. Each grid cell was characterized using the dominant topsoil (D1) layer of the corresponding Soil Mapping Unit. USDA soil texture codes, based on the relative proportions of sand, silt and clay, were first mapped to the 12 standard USDA textural classes [49] and then aggregated into three broader texture groups: (i) sandy (sand, loamy sand, sandy loam), (ii) silty (silt, silt loam, loam), and (iii) clayey (clay, silty clay, sandy clay, clay loam, silty clay loam, sandy clay loam). Grid cells corresponding to open water bodies or lacking valid soil information were masked. Because biomass burning is an important non-agricultural source of atmospheric NH_3 [32], fire-related NH_3 emissions were quantified using the Copernicus Atmospheric Monitoring System (CAMS) Global Fire Assimilation System (GFAS), which estimates emissions from fire radiative power [30]. GFAS daily NH_3 fluxes for 2008–2023 were converted to mean annual totals and re-gridded to the common $1/12^\circ$ framework. To minimize the influence of biomass burning, only regions with a mean annual fire-related NH_3 flux below 1×10^{-5} kg m^{-2} yr^{-1} (0.1 kg NH_3 ha^{-1} yr^{-1}) were retained. In addition, months of peak fire activity, defined as those in which the mean monthly fire-related NH_3 flux exceeded the regional 80^{th} percentile, were excluded from the analysis, both from the annual curves and the monthly ones.

To ensure comparability across a broad temperature range, the analysis focused on warm agricultural regions where daily T_{skin} frequently exceeded 310 K. To restrict the analysis to NH_3-rich environments, only grid cells with mean NH_3 column densities above 3×10^{15} molec.cm^{-2}, averaged over 2008–2023, were retained. Both criteria were derived from IASI observations. Based on these combined constraints, nine agricultural regions were selected for detailed analysis (Fig. 1). Six correspond to urea-dominated systems, including three sites in South Asia, the world's largest urea-consuming region, accounting for nearly one-third of global urea use [21]; the additional urea-dominated regions are located in Nigeria, Egypt and Sudan. Three non-urea dominated regions (urea contribution below 40%) were selected in southern Spain, the central United States of America and Morocco, each representing a distinct dominant soil texture class. Table 1 summarizes the key characteristics of the core regions. To further test our interpretation, we analyzed additional agricultural regions based exclusively on their urea contribution, with comprehensive data for all sites detailed in Supplementary Tables 1–3.

Drought–rewetting analysis

To investigate drought–rewetting dynamics in South Asian region A, IASI NH_3 and T_{skin} observations were complemented with rainfall and soil moisture datasets. Precipitation was obtained from the CHIRPS v3 dataset (Climate Hazards Group InfraRed Precipitation with Station data), using the global pentad product, which provides 5-day accumulated precipitation totals at 0.05° resolution from 2008 to 2023 [39]. CHIRPS combines infrared satellite-derived precipitation estimates with *in situ* rain gauge observations to generate spatially complete rainfall fields, and has been extensively validated for its ability to capture seasonal rainfall variability and extreme precipitation events across data-sparse regions, including South Asia. Soil moisture was taken from the ESA Climate Change Initiative (CCI) COMBINED surface soil moisture product (v09.1), which provides daily estimates at 0.25° resolution as volumetric water content (m^3 m^{-3}) [38]. All datasets were spatially aggregated over the predefined bounding box of region A without pixel-level regridding, thereby preserving their native resolution. IASI NH_3 and T_{skin} retrievals were treated as point observations and aggregated into fixed 5-day (pentad) bins, from which mean NH_3 columns and mean T_{skin} were calculated. CHIRPS precipitation totals were spatially averaged over the region for each pentad, while ESA CCI soil moisture fields were spatially averaged over the same region and then aggregated into pentads by computing the mean within each 5-day interval. Pentad bins were aligned identically across all datasets to ensure temporal consistency, suppress day-to-day variability, and preserve drought–rewetting transitions, thereby enabling direct comparison of rainfall, soil moisture, temperature, and NH_3 variability.

Data availability

The IASI NH_3 (ANNI v4) and T_{skin} products are available from the AERIS data centre (https://iasi.aeris-data.fr). CHIRPS v3 precipitation, ESA CCI soil moisture (v09.1), GLC-SHARE, HWSD v2.0, CAMS-GFAS and IFASTAT fertilizer statistics are available from their respective providers as cited in the Methods.

Code availability

The analysis code used to construct the NH_3–T_{skin} relationships and to derive the breakpoint temperature (T_b) and Q_{10} values is publicly available on Zenodo at https://doi.org/10.5281/zenodo.23163582 under the MIT licence.

Acknowledgements

The present research is part of the Space4Relaunch project, supported by the SPW Économie Emploi Recherche of the Walloon Region under grant agreement number 2210181. Additional support was provided through the “Hyperspectral atmospheric IR sounding missions” (HIRS) project and by the Fondation ULB. L.C. is a senior research associate supported by the FRS-FNRS. M.A.S. gratefully acknowledges support for

the International Nitrogen Management System (INMS) through the GEF/UNEP 'Towards INMS' project.

Author contributions

P.C., M.V.D., and L.C. established the foundational IASI NH_3–T_{skin} observational framework, made the initial observations and supervised the study. M.R. led the specific study design, executed the data analysis, formulated the mechanistic interpretation, and wrote the manuscript. M.A.S. provided expertise on global agronomy, fertilizer management, and NH_3 volatilization parameterizations. C.C. provided insights on the IASI satellite methodology and data processing. C.V. and A.-C.R. contributed to the interpretation of atmospheric chemistry and spatiotemporal NH_3 variability. All authors provided crucial feedback on the methodology, discussed the findings, and contributed to editing the manuscript.

Competing interests

The authors declare no competing interests.

References

[1] Erisman, J. W., Sutton, M. A., Galloway, J., Klimont, Z. & Winiwarter, W. How a century of ammonia synthesis changed the world. *Nature Geoscience* **1**, 636–639 (2008).

[2] Sutton, M. A. *et al.* *Our Nutrient World: The Challenge to Produce More Food and Energy with Less Pollution* (Centre for Ecology and Hydrology, Edinburgh, on behalf of the Global Partnership on Nutrient Management and the International Nitrogen Initiative, 2013).

[3] Behera, S. N., Sharma, M., Aneja, V. P. & Balasubramanian, R. Ammonia in the atmosphere: A review on emission sources, atmospheric chemistry and deposition on terrestrial bodies. *Environmental Science and Pollution Research* **20**, 8092–8131 (2013).

[4] Viatte, C. *et al.* Atmospheric ammonia variability and link with particulate matter formation: A case study over the Paris area. *Atmospheric Chemistry and Physics* **20**, 577–596 (2020).

[5] GBD 2021 Risk Factors Collaborators. Global burden and strength of evidence for 88 risk factors in 204 countries and 811 subnational locations, 1990–2021: a systematic analysis for the Global Burden of Disease Study 2021. *The Lancet* **403**, 2162–2203 (2024).

[6] Dirnböck, T. *et al.* Forest floor vegetation response to nitrogen deposition in Europe. *Global Change Biology* **20**, 429–440 (2014).

[7] Stevens, C. J. *et al.* Nitrogen deposition threatens species richness of grasslands across Europe. *Environmental Pollution* **158**, 2940–2945 (2010).

[8] Van Damme, M. *et al.* Global, regional and national trends of atmospheric ammonia derived from a decadal (2008–2018) satellite record. *Environmental Research Letters* **16**, 055017 (2021).

[9] Nemitz, E., Sutton, M. A., Schjoerring, J. K., Husted, S. & Wyers, G. P. Resistance modelling of ammonia exchange over oilseed rape. *Agricultural and Forest Meteorology* **105**, 405–425 (2000).

[10] Roelle, P. A. & Aneja, V. P. Characterization of ammonia emissions from soils in the upper coastal plain, North Carolina. *Atmospheric Environment* **36**, 1087–1097 (2002).

[11] Sutton, M. A., Asman, W. A. H. & Schjørring, J. K. Dry deposition of reduced nitrogen. *Tellus B* **46**, 255–273 (1994).

[12] Krichels, A. H. *et al.* Soil NH_3 emissions across an aridity, soil pH, and N deposition gradient in southern California. *Elementa: Science of the Anthropocene* **11**, 00123 (2023).

[13] Sutton, M. A. *et al.* Towards a climate-dependent paradigm of ammonia emission and deposition. *Philosophical Transactions of the Royal Society B: Biological Sciences* **368**, 20130166 (2013).

[14] Skjøth, C. A., Hertel, O., Gyldenkærne, S. & Ellermann, T. Implementing a dynamical ammonia emission parameterization in the large-scale air pollution model ACDEP. *Journal of Geophysical Research: Atmospheres* **109**, D06306 (2004).

[15] Beaudor, M. *et al.* Global agricultural ammonia emissions simulated with the ORCHIDEE land surface model. *Geoscientific Model Development* **16**, 1053–1081 (2023).

[16] Vira, J., Hess, P., Melkonian, J. & Wieder, W. R. An improved mechanistic model for ammonia volatilization in Earth system models: Flow of Agricultural Nitrogen, version 2 (FANv2). *Geoscientific Model Development* **13**, 4459–4490 (2020).

[17] Jiang, J., Stevenson, D. S. & Sutton, M. A. A dynamical process-based model for quantifying global agricultural ammonia emissions: AMmonia–CLIMate v1.0 (AMCLIM v1.0), Part 1: Land module for simulating emissions from synthetic fertilizer use. *Geoscientific Model Development* **17**, 8181–8222 (2024).

[18] Manders, A. M. M. *et al.* Curriculum vitae of the LOTOS-EUROS (v2.0) chemistry transport model. *Geoscientific Model Development* **10**, 4145–4173

(2017).

[19] Abeed, R. *et al.* A roadmap to estimating agricultural ammonia volatilization over Europe using satellite observations and simulation data. *Atmospheric Chemistry and Physics* **23**, 12505–12523 (2023).

[20] Cantarella, H., Otto, R., Soares, J. R. & Brito Silva, A. G. Agronomic efficiency of NBPT as a urease inhibitor: A review. *Journal of Advanced Research* **13**, 19–27 (2018).

[21] International Fertilizer Association. Global consumption of synthetic nitrogen fertilizers per country (2024). URL https://www.ifastat.org/. IFASTAT Plant Nutrition Database. Accessed 24 April 2025.

[22] Eyring, H. The activated complex in chemical reactions. *The Journal of Chemical Physics* **3**, 107–115 (1935).

[23] Feder, M. J., Akyel, A., Morasko, V. J., Gerlach, R. & Phillips, A. J. Temperature-dependent inactivation and catalysis rates of plant-based ureases for engineered biomineralization. *Engineering Reports* **3**, e12299 (2021).

[24] Wallenstein, M. D., Allison, S. D., Ernakovich, J., Steinweg, J. M. & Sinsabaugh, R. L. Controls on the temperature sensitivity of soil enzymes: a key driver of in situ enzyme activity rates. in *Soil Enzymology* (eds Shukla, G. & Varma, A.) Soil Biology Vol. 22, 245–258, Springer, Berlin, Heidelberg (2011).

[25] Mekonnen, E., Kebede, A., Nigussie, A., Kebede, G. & Tafesse, M. Isolation and characterization of urease-producing soil bacteria. *International Journal of Microbiology* **2021**, 8888641 (2021).

[26] O'Toole, P. & Morgan, M. A. Thermal stabilities of urease enzymes in some Irish soils. *Soil Biology and Biochemistry* **16**, 471–474 (1984).

[27] Clarisse, L. *et al.* The IASI NH_3 version 4 product: Averaging kernels and improved consistency. *Atmospheric Measurement Techniques* **16**, 5009–5028 (2023).

[28] Latham, J., Cumani, R., Rosati, I. & Bloise, M. Global Land Cover SHARE (GLC-SHARE) database beta-release version 1.0 (2014). FAO, Rome.

[29] FAO & IIASA. Harmonized World Soil Database version 2.0 (HWSD v2.0) (2023). FAO, Rome / IIASA, Laxenburg.

[30] Kaiser, J. W. *et al.* Biomass burning emissions estimated with a global fire assimilation system based on observed fire radiative power. *Biogeosciences* **9**, 527–554 (2012).

[31] Sommer, S. G., Schjørring, J. K. & Denmead, O. T. Ammonia emission from mineral fertilizers and fertilized crops. *Advances in Agronomy* **82**, 557–622 (2004).

[32] Whitburn, S. *et al.* Ammonia emissions in tropical biomass burning regions: Comparison between satellite-derived emissions and bottom-up fire inventories. *Atmospheric Environment* **121**, 42–54 (2015).

[33] Feng, T. *et al.* Soil urease activity is mediated more by *ureC* microbial diversity in wet regions than dry regions: Key roles of generalist-abundant and -rare species. *Functional Ecology* **39**, 2015–2028 (2025).

[34] Van Damme, M. *et al.* Global distributions, time series and error characterization of atmospheric ammonia (NH_3) from IASI satellite observations. *Atmospheric Chemistry and Physics* **14**, 2905–2922 (2014).

[35] Schimel, J. P. Life in dry soils: Effects of drought on soil microbial communities and processes. *Annual Review of Ecology, Evolution, and Systematics* **49**, 409–432 (2018).

[36] Wallenstein, M. D., McMahon, S. K. & Schimel, J. P. Seasonal variation in enzyme activities and temperature sensitivities in Arctic tundra soils. *Global Change Biology* **15**, 1631–1639 (2009).

[37] Bogati, K. A., Sewerniak, P. & Walczak, M. Unraveling the effect of soil moisture on microbial diversity and enzymatic activity in agricultural soils. *Microorganisms* **13**, 1245 (2025).

[38] Dorigo, W. *et al.* ESA Soil Moisture Climate Change Initiative (Soil Moisture CCI): COMBINED product, version 09.1 (2024). NERC EDS Centre for Environmental Data Analysis.

[39] Funk, C. *et al.* The Climate Hazards Center infrared precipitation with stations, version 3. *Scientific Data* **13**, 718 (2026).

[40] Birch, H. F. The effect of soil drying on humus decomposition and nitrogen availability. *Plant and Soil* **10**, 9–31 (1958).

[41] Borken, W. & Matzner, E. Reappraisal of drying and wetting effects on C and N mineralization and fluxes in soils. *Global Change Biology* **15**, 808–824 (2009).

[42] Montes, C., Urfels, A. & Han, E. Planting rice at monsoon onset could mitigate the impact of temperature stress on rice–wheat systems of Bihar, India. *Atmosphere* **14**, 40 (2023).

[43] Vatta, K. *et al.* Assessing the economic impact of a low-cost water-saving irrigation technology in Indian Punjab: The tensiometer. *Water International* **43**, 305–321 (2018).

[44] Clerbaux, C. *et al.* Monitoring of atmospheric composition using the thermal infrared IASI/MetOp sounder. *Atmospheric Chemistry and Physics* **9**, 6041–6054 (2009).

[45] Clarisse, L., Clerbaux, C., Dentener, F., Hurtmans, D. & Coheur, P.-F. Global ammonia distribution derived from infrared satellite observations. *Nature Geoscience* **2**, 479–483 (2009).

[46] Van Damme, M. *et al.* Industrial and agricultural ammonia point sources exposed. *Nature* **564**, 99–103 (2018).

[47] Franco, B. *et al.* A general framework for global retrievals of trace gases from IASI: Application to methanol, formic acid, and PAN. *Journal of Geophysical Research: Atmospheres* **123**, 13963–13984 (2018).

[48] Di Gioacchino, T. *et al.* Spatial and temporal variations of thermal contrast in the planetary boundary layer. *Journal of Remote Sensing* **4**, 0142 (2024).

[49] Groenendyk, D. G., Ferré, T. P. A., Thorp, K. R. & Rice, A. K. Hydrologic-process-based soil texture classifications for improved visualization of landscape function. *PLoS ONE* **10**, e0131299 (2015).

Supplementary Files

This is a list of supplementary files associated with this preprint. Click to download.

- SupplementaryInformationRosiersetal.pdf